Geomorphology 282 (2017) 150–161

Contents lists available at ScienceDirect

Geomorphology

journal homepage: www.elsevier.com/locate/geomorph

A morphologic proxy for debris flow erosion with application to the earthquake deformation cycle, Cascadia Subduction Zone, USA

Brian D. Penserini [a], Joshua J. Roering [a,*], Ashley Streig [b]

[a] Department of Earth Sciences, University of Oregon, Eugene, Oregon, 97403-1272, USA
[b] Department of Geology, Portland State University, Portland, Oregon, 97201, USA

ARTICLE INFO

Article history:
Received 1 August 2016
Received in revised form 11 January 2017
Accepted 12 January 2017
Available online 16 January 2017

Keywords:
debris flows
earthquakes
coseismic subsidence
LiDAR
valley networks
longitudinal profile
slope-area data

ABSTRACT

In unglaciated steeplands, valley reaches dominated by debris flow scour and incision set landscape form as they often account for >80% of valley network length and relief. While hillslope and fluvial process models have frequently been combined with digital topography to develop morphologic proxies for erosion rate and drainage divide migration, debris-flow-dominated networks, despite their ubiquity, have not been exploited for this purpose. Here, we applied an empirical function that describes how slope-area data systematically deviate from so-called fluvial power-law behavior at small drainage areas. Using airborne LiDAR data for 83 small (~1 km^2) catchments in the western Oregon Coast Range, we quantified variation in model parameters and observed that the curvature of the power-law scaling deviation varies with catchment-averaged erosion rate estimated from cosmogenic nuclides in stream sediments. Given consistent climate and lithology across our study area and assuming steady erosion, we used this calibrated denudation-morphology relationship to map spatial patterns of long-term uplift for our study catchments. By combining our predicted pattern of long-term uplift rate with paleoseismic and geodetic (tide gauge, GPS, and leveling) data, we estimated the spatial distribution of coseismic subsidence experienced during megathrust earthquakes along the Cascadia Subduction Zone. Our estimates of coseismic subsidence near the coast (0.4 to 0.7 m for earthquake recurrence intervals of 300 to 500 years) agree with field measurements from numerous stratigraphic studies. Our results also demonstrate that coseismic subsidence decreases inland to negligible values >25 km from the coast, reflecting the diminishing influence of the earthquake deformation cycle on vertical changes of the interior coastal ranges. More generally, our results demonstrate that debris flow valley networks serve as highly localized, yet broadly distributed indicators of erosion (and rock uplift), making them invaluable for mapping crustal deformation and landscape adjustment.

1. Introduction

In hilly and mountainous landscapes, changes in base level driven by rock uplift influence the shape of river longitudinal and hillslope profiles through process-form feedbacks. Given sufficient time, erosion tends to balance rock uplift such that steady state (or time invariant) conditions result (Mackin, 1948; Fernandes and Dietrich, 1997; Whipple and Tucker, 1999). Hillslope angles and the convexity of hilltops have been shown to provide quantitative constraints on the pace of base level lowering induced by uplift (Hurst et al., 2012; Sweeney et al., 2015; Mudd, 2016), and the characteristic concave form of fluvial longitudinal profiles has been frequently exploited to extract information on tectonic forcing in a vast array of geologic settings (Hack, 1973; Kirby and Whipple, 2001; Wobus et al., 2006; Perron and Royden, 2013; Cyr et al., 2010).

For stream networks in particular, the oft-observed inverse power-law dependence of drainage area on valley slope is consistent with stream power models of fluvial bedrock incision (Howard and Kerby, 1983; Whipple and Tucker, 1999; Lague, 2014). This functional relationship that relates longitudinal profiles to erosion (and uplift) allows spatial variations in tectonic forcing to be inferred from examination of readily available topographic information (Ahnert, 1970; Howard and Kerby, 1983; Milliman and Syvitski, 1992; Dietrich et al., 2003; Binnie et al., 2007). While the form of the stream power law states that incision rate is equivalent to the power law product of channel slope and drainage area (Whipple, 2004), alternative parameter-rich incision models demonstrate that concave power-law profiles also emerge from abrasion and plucking mechanisms that account for the opposing roles of fluvial sediments in providing tools for incision and coverage of stream beds (Sklar and Dietrich, 2004; Chatanantavet and Parker, 2009; Gasparini and Brandon, 2011; Shobe et al., 2016). While these sophisticated models are deemed physically relevant and have been supported by experiments (Sklar and Dietrich, 2001; Finnegan et al., 2007), their application for the interpretation of natural landscapes has yet to be

* Corresponding author.
E-mail address: jroering@uoregon.edu (J.J. Roering).

http://dx.doi.org/10.1016/j.geomorph.2017.01.018
0169-555X/

realized, with a few exceptions (Attal et al., 2011; Gasparini and Brandon, 2011; Hobley et al., 2011; Sweeney and Roering, 2016). Rather, the stream power model has proven to be accessible and easily digestible for tasks such as mapping patterns of channel steepness and identifying the signature of transient adjustment (Crosby and Whipple, 2006; Whittaker et al., 2007; Mudd, 2016; Willett et al., 2014). The normalized slope of fluvial networks, termed the *steepness index*, can be extracted from slope-area data given constant concavity (i.e., constant power-law scaling) and has been shown to vary systematically with erosion rate (e.g., Lague et al., 2000; Snyder et al., 2000; Ouimet et al., 2009; DiBiase et al., 2010; Kirby and Whipple, 2012; Harel et al., 2016).

While these network analyses have proven to be astonishingly effective reconnaissance tools for detecting spatial and temporal variations in deformation and erosion, their scope may be limited to the fluvial-dominated portion of channel networks. Thus far, these analyses assume constant power-law scaling of slope-area data, and as a result their relevance for characterizing low-drainage area (or steep headwaters) portions of drainage basins is unclear. In these upper reaches of unglaciated mountainous catchments, the scaling often systematically deviates from constant concavity. Instead, valley slope angles tend to approach a threshold value set by the stability of colluvial hollows (Stock and Dietrich, 2003) and unconsolidated, in-channel sediment deposits (McCoy et al., 2012; Kean et al., 2013; Prancevic et al., 2014) that serve as the initiation zones for debris flows that transverse significant portions of the downstream network. Given the absence of significant fluvial transport (much less incision) in these areas (Fig. 1) that represent the transition between hillslopes and the channelized portions of networks (Montgomery and Buffington, 1997; Lague and Davy, 2003), debris flows typically are implicated as the primary incision process in so-called *colluvial valleys* (Dietrich and Dunne, 1978; Benda, 1990; Stock and Dietrich, 2003, 2006).

These steep, debris-flow-dominated reaches are typically found at relatively small drainage areas (<1 to 5 km^2) that often constitute >80% of the regional topographic relief (Stock and Dietrich, 2003). The transition between debris flow and fluvial-dominated portions of the drainage network is often debated as Stock and Dietrich (2006) reported that debris flow deposits overlap with the upstream extent of fluvial strath terraces in the Pacific Northwest. In the San Gabriel Mountains of southern California, debris flows frequently traverse the entire drainage network of many catchments before being arrested by engineered debris basins dotted along the range front to mitigate the hazard (Lavé and Burbank, 2004), although field observations reveal features characteristic of fluvial incision in some upstream reaches (DiBiase et al., 2012).

Fig. 1. Debris flow catchments. This oblique aerial photo (photo by J. Roering) shows characteristic debris-flow-dominated catchments in the Oregon Coast Range. Yellow outline delineates catchment boundaries while the dotted white lines illustrate the primary debris flow tracks that terminate in unchanneled valleys just below the ridgetops.

The morphology of debris-flow-dominated (or colluvial) profiles tends to be steeper and less concave than predicted by fluvial power-law scaling and instead approach a constant slope at very small drainage areas (~10^3 m^2), coincident with unchanneled valleys. It has been proposed that these colluvial reaches can be described by the concatenation of numerous power law relationships (Lague and Davy, 2003; Whipple and Tucker, 1999; DiBiase et al., 2012). In many settings, high-resolution laser altimetry reveals a smoothly varying (or curved) log-log slope-area topographic signature for debris flow valleys (Stock and Dietrich, 2003, 2006). Stock and Dietrich (2003) developed an empirical function for debris flow slope-area data, and their three-parameter function described the continuous transition from relatively constant slope angles (similar to threshold slopes) observed at small drainage areas to the inverse power law relationship of fluvial channels at larger drainage areas. Stock and Dietrich (2003) postulated that as erosion rates increase, the profile of steep, debris flow valleys lengthens, forcing the transition from debris flow to fluvial-dominated reaches to occur farther downstream in larger drainage areas. The mechanical model of Stock and Dietrich (2006) posited that valley slope (and the characteristic curved slope-area signature of steepland headwaters) results from the balance between processes that *increase* incision in the downvalley direction (such as increasing flow event frequency and sediment entrainment) and processes that *decrease* incision downstream (such as lower inertial stresses from lower slope angles and the prevalence of less weathered, more coherent bedrock). A recent theoretical contribution adopted a similar framework for general landscape and network evolution (Shelef and Hilley, 2016).

Given topographic data of sufficient resolution, small and ubiquitous debris flow catchments have the potential to serve as highly localized and broadly dispersed recorders of rock uplift that adjust rapidly to changes in tectonic forcing (Hurtrez et al., 1999). In this contribution, we explore whether the shape of debris flow valley profiles can be used to interpret patterns of erosion and rock uplift in active orogens. Specifically, we seek to reconcile long-term uplift patterns with the earthquake deformation cycle in the Pacific Northwest, where large megathrust events associated with the Cascadia Subduction Zone have occurred every 300-600 years during the Holocene (Goldfinger et al., 2012). These events result in substantial coseismic subsidence (>0.5 m) in coastal settings (Graehl et al., 2015), but the inland extent of this deformation that may reflect the geometry of plate locking and coseismic slip is unknown. By combining modern interseismic uplift data with estimates of earthquake recurrence intervals and our analysis of long-term uplift generated by debris flow network morphometry, we propose a means to predict the pattern of coseismic subsidence along the Pacific Northwest coastal ranges. This endeavor also begins to confront the role of earthquakes in the evolution of Cascadia landscapes, which has not been addressed despite abundant geomorphic research in the region.

2. Tectonic forcing and valley network morphology

2.1. Stream power and steepness index for fluvial networks

Fluvial channels typically exist at drainage areas >0.5 to 1 km^2 in steepland catchments, often associated with valley slopes <0.05 to 0.15 (Lague et al., 2000; Stock and Dietrich, 2003). In these reaches, the relationship between incision rate, channel slope, and drainage area is often expressed by the stream power law

$$E = KA^mS^n \quad (1)$$

where E is the rate of bedrock channel incision, K is the incision coefficient, A is drainage area, S is local channel slope, and m and n are empirically derived constants (Whipple, 2004). This form of the stream power law is practical as it is formulated in terms of local channel slope and upstream drainage area, two parameters that are easily estimated from digital elevation models (DEMs). Furthermore, given steady erosion (i.e., uplift = erosion), the stream power model can be recast

with slope decreasing as a power law function of drainage area, wherein the coefficient incorporates uplift rate (U):

$$S = (U/K)^{1/n} A^{m/n} \quad (2)$$

This formulation is frequently used to map channel steepness with the following expression referred to as Flint's Law (Flint, 1974):

$$S = k_s A^{-\theta} \quad (3)$$

where $k_s = (U/K)^{1/n}$ is referred to as the channel steepness index with units equal to $L^{2\theta}$ (Snyder et al., 2000), and $\theta = m/n$ is the concavity. This form of the stream power law produces a linear trend in log-log slope-area space, given steady, uniform erosion and constant K. Several studies have examined variability in k_s and θ for catchments with uplift rate being the only known variable, and their findings indicate that θ does not systematically vary with uplift rate (Wobus et al., 2006; Kirby and Whipple, 2012). Meanwhile, k_s is very sensitive to changes in uplift (Lague et al., 2000; Snyder et al., 2000; Kirby and Whipple, 2001; Duvall et al., 2004). Because the units of k_s depend on the corresponding θ value, a fixed value of θ called the reference concavity, θ_{ref}, typically is used in order to compare steepness indices between profiles (or networks), and the k_s value that results from the best fitting power law with $\theta = \theta_{ref}$ is called the normalized channel steepness index, k_{sn}. Many linear (and nonlinear) relationships between erosion rate and normalized channel steepness have been proposed (Snyder et al., 2000, 2003; Kirby and Whipple, 2001; Lague and Davy, 2003; Duvall et al., 2004; Binnie et al., 2007; Harkins et al., 2007; Ouimet et al., 2009; Cyr et al., 2010; DiBiase et al., 2010; Kirby and Whipple, 2012; Harel et al., 2016).

2.2. Debris flow-dominated networks

At low drainage areas, the relationship between slope and area deviates from the power law trend associated with fluvial regions (Fig. 2). These reaches are often characterized by a curved relationship in log-log slope-area space, representing a continuous (rather than discrete) scaling break from the power law fluvial relationship (Stock and Dietrich, 2003, 2006). The function proposed by Stock and Dietrich (2003) to represent the slope-area relationship for debris flow valleys was given by

$$S = S_0/(1 + a_1 A^{a2}) \quad (4)$$

where S_0 represents valley head slope (slope at negligible drainage area), a_1 is an empirical constant (with units of $1/(\text{length}^2)^{a2}$) that is inversely proportional to the curvature of the log-log trend and represents the sharpness of the scaling transition, and a_2 is a unitless empirical constant analogous to θ in that it represents the power law slope at large drainage areas (Stock and Dietrich, 2003). Stock and Dietrich (2003) recognized that these three parameters can account for curved slope-area relationships from debris-flow-dominated reaches in diverse geologic settings. This function converges to a constant slope ($S \sim S_0$) at small drainage areas and to an inverse power law (defined by fluvial scaling exponent or concavity) at large drainage areas ($S \sim (S_0/a_1 A^{a2})$) and thus emulates the transition between hillslope and fluvial regimes that we observe in natural landscapes. Because S_0 is likely set by soil transport rates on steep sideslopes and shallow landslide and sediment entrainment mechanics in steep unchanneled valley axes, it may be somewhat insensitive to variations in uplift (or erosion) rate and instead reflect the shear strength of coarse, unconsolidated soil (Prancevic et al., 2014) and soils that may be reinforced by dense root networks (Schmidt et al., 2001). Our application does not require that S_0 be invariant with uplift or erosion rate; instead, we seek to test this assertion. Additionally, a_2 is not expected to vary with uplift rate in the absence of systematic variation in lithology, basin geometry, and climate (Harel et al., 2016).

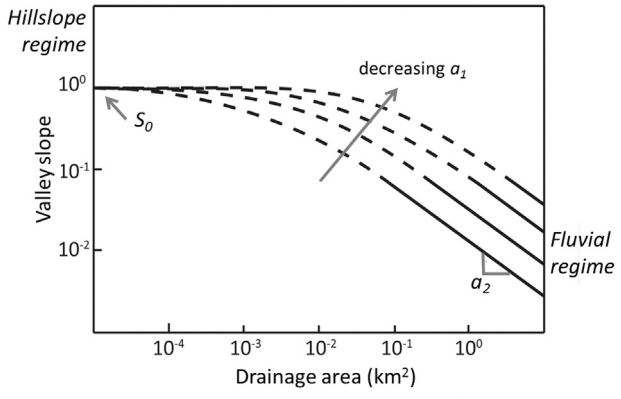

Fig. 2. Debris flow network morphology. Schematic plot of drainage area vs. valley slope for forested, steepland catchments. At small areas, slope angles are relatively invariant and set by threshold-driven debris flow initiation processes. At large drainage areas, slope varies as an inverse power law with area, reflecting fluvial-dominated erosion and valley maintenance. Intermediate areas in this plot represent debris flow-dominated terrain wherein a curved slope-area relationship connects the hillslope and fluvial domain. The parameters of Eq. (4) are shown for illustration; the value of a_1 represents the curvature or sharpness of the transition and is proposed to correlate with erosion (or uplift) rate.

Stock and Dietrich (2003) inferred a potential correlation between a_1, which can be conceptualized as the convexity (or span) of the power law scaling transition between the debris flow and fluvial portions of slope-area relationships, and rock uplift rate and lithology. Using data collected from 12 regions of similar lithology in the U.S., they noted that as uplift rate increases, a_1 has a propensity to decrease and, thus, curvature of the slope-area relation tends to increase (Fig. 2). They hypothesized that as uplift rate increases, steep, debris-flow-prone valley reaches migrate to larger drainage areas in a manner similar to the responses of coupled hillslope-fluvial systems in the simulations of Howard (1997) and Tucker and Bras (1998). Farther downstream, valley slopes begin to decrease as debris-flow-dominated reaches transition to channelized fluvial reaches (Fig. 2). Debris flows in the confined valleys of this transitional realm tend to deposit at slopes of ~0.03-0.1 as they are unable to overcome the forces resisting downslope movement (Stock and Dietrich, 2003, 2006; Hsu et al., 2008). This physical limit may correspond with the lower extent of the curved slope-area relation, and this transition is dictated by the debris flow and fluvial regimes that co-occur here. Thus, increasing rock uplift rate potentially shifts debris flow valley slopes to larger drainage areas at the expense of fluvial reaches, which effectively concentrates long-profile and slope-area curvature downstream and produces a more abrupt transition that is reflected by lower a_1 values (Fig. 2). Alternatively, one can interpret the slope-area regime depicted in Fig. 2 in terms of increasing uplift rate that causes the fluvial realm (power law portion of the network) to shift to the right in slope-area space (which is equivalent to increasing the steepness index, k_{sn}), resulting in steeper valley slopes associated with debris flow processes to migrate downstream.

3. Study area: central Oregon Coast Range

The bedrock of the central Oregon Coast Range (OCR) is largely composed of the Eocene Tyee Formation, an ~3-km-thick, sand-rich sequence of turbidites with gently dipping, undeformed strata of relatively uniform lithology (Baldwin, 1956; Dietrich and Dunne, 1978; Heller and Dickinson, 1985; Reneau and Dietrich, 1991; Snavely et al., 1964). East-west facies variability is minimal, but a south-to-north reduction in formation thickness and sandstone to siltstone ratio has been noted owing to the orientation of the delta-fed submarine margin at the time of deposition (Heller and Dickinson, 1985). Oligocene gabbroic dikes manifest locally as east-west oriented high-elevation ridges because of their high resistance to erosion, although these features account for <5% of the mapped surface exposure in the region. Uplift of the OCR was initiated in the Miocene and is driven by subduction of the Juan de Fuca plate along the Cascadia Subduction Zone, located 60 to 100 km west of the Oregon coast (McNeill et al., 2000). Positive net uplift continues today along much of the coast as

evidenced by prominent marine terraces with long-term uplift rates ranging from 0.1 to >0.4 mm/y (Kelsey et al., 1996). Additionally, long-term uplift rates interpreted from strath terraces throughout the central OCR also range from 0.1 to 0.3 mm/y (Personius, 1995), although the applicability of terrace incision records for interpreting uplift is a topic of vigorous debate (Finnegan et al., 2014; Gallen et al., 2015).

The Cascadia Subduction Zone experienced >20 large magnitude ($M_w = 8$ to 9+) earthquakes in the Holocene, and many of these events have been shown to rupture from northern California to British Columbia (Goldfinger et al., 2012). These earthquakes generate coseismic subsidence along the Oregon coast that is estimated to be 0.4 to 1.0 m based on analyses from estuaries and other coastal settings (Witter et al., 2003; Leonard et al., 2010; Graehl et al., 2015). Since the last major megathrust rupture in A.D. 1700, most coastal areas in this region have experienced interseismic uplift that exceeds long-term rock uplift and erosion by >10 times (Kelsey et al., 1994; Burgette et al., 2009). The prevalence of progressively uplifted marine terraces along much of the southern and central Oregon coast implies that interseismic strain is not fully recovered during megathrust events (Kelsey et al., 1994), although the source of permanent uplift is currently debated and mechanisms include buoyancy associated with young oceanic crust and sediment underplating (Audet et al., 2010).

Our analysis focuses on an east-west swath in the central Oregon Coast Range; a humid, unglaciated, forested, soil-mantled, mountainous landscape characterized by steep topography and relatively evenly spaced ridges and valleys. In this region, shallow landslides tend to originate from colluvial (or unchanneled valleys) and often translate into far-traveled debris flows (Dietrich and Dunne, 1978). The portion of the valley network dominated by debris flow scour and incision substantially influences landscape form, accounting for >80% of network length as well as the vast majority of valley network relief (Benda and Dunne, 1997; Stock and Dietrich, 2003). Debris flows tend to terminate upstream of channel slopes of ~0.03 to 0.1, where step-pool bedforms begin to appear and fluvial processes become dominant (Montgomery and Buffington, 1997; Stock and Dietrich, 2006).

Erosion rate estimates derived from several methods (including suspended sediment yield, colluvial sediment flux, cosmogenic radionuclides, and radiocarbon) suggest values that cluster around 0.1 mm/y throughout the central OCR (Beschta, 1978; Reneau and Dietrich, 1991; Bierman et al., 2001; Heimsath et al., 2001). This correspondence of long-term uplift and erosion rates implies that the central OCR may approximate steady state over timescales of $>10^4$ years, although recent paleo-erosion analyses indicate that glacial-interglacial climate fluctuations generate erosion rate variations of 2 to 3 times (Marshall et al., 2015). Our analysis does not account for these temporal variations but instead notes that such fluctuations would similarly affect all of our study catchments and thus not impact the spatial patterns in catchment morphology that we document below. In addition, our study sites avoid transience (temporally and spatially) that result from deep-seated landslides, drainage capture and reorganization, and differential stream incision associated with rock strength variations and bedrock meandering (Roering et al., 2005; vanLaningham et al., 2006; Almond et al., 2007; Marshall and Roering, 2014).

4. Methods

4.1. Topographic analysis

The prevalence of steep headwater catchments, relatively uniform lithology, and sufficient time to achieve an approximate balance between long-term uplift and erosion rates recommends the Oregon Coast Range as a promising study area to extract incision rate information from debris flow-dominated valley networks. Using high-resolution, 1-m airborne laser altimetry (LiDAR) data acquired by the Oregon Department of Geology and Mineral Industries (DOGAMI), we applied Stock and Dietrich's (2003) empirical function to 83 catchments with drainage area between 0.4 and 3.0 km^2. We selected catchments concentrated in a region surrounding the outlet of the Umpqua River on the Oregon Coast (Fig. 3). No Quaternary active faults have been mapped in the study area, and the region is minimally folded (Fig. 3) (U.S. Geological Survey, 2006; Marshall and Roering, 2014). We avoided large catchments as well as catchments where hillslope or valley profile morphology appears to be influenced by transient base level lowering, such as dike-controlled knickpoints and deep-seated landslides, both of which are rare in this region of the coastal ranges.

We extracted the valley network from each catchment using TopoToolbox 2, a MATLAB-based geoprocessing toolbox, with a minimum drainage area of 250 m^2 (Schwanghart and Scherler, 2013). This threshold corresponds to the downslope extent of the hillslope regime and the onset of shallow landsliding in topographic hollows (Roering, 2008). Valley network elevations were smoothed using a 15-m smoothing window (Roering et al., 2010) with a first-order Savitzky-Golay filter and local slopes and drainage areas were calculated from the resulting smoothed network. Slope and drainage area values were log-transformed and binned to reduce the overwhelming number of data points in each catchment. The slope-area data sets for each of the 83 catchments were then fit with Eq. (4) using the MATLAB Curve Fitting Toolbox. Each binned data point was weighted by the number of measurements included in that bin (Stock and Dietrich, 2003). Best-fit parameters (a_1, a_2, and S_0) for each catchment, as well as their 95% confidence intervals, degrees of freedom, and r^2 values, were recorded. We identified catchments with low r^2 values (<0.85) and visually inspected them for the presence of transient or other anomalous topographic signatures. This filtering resulted in the elimination of five catchments.

We plotted the distributions of a_1, a_2, and S_0 and quantified the variance of these morphologic parameters within our study group. Because values of a_1 covary with a_2, we used a reference value approach similar to that used in studies of the normalized channel steepness (k_{sn}) in order to compare a_1 values between our study catchments (Lague et al., 2000; Snyder et al., 2000; Kirby and Whipple, 2001; Duvall et al., 2004). Following Wobus et al. (2006), we determined the reference a_2 value to be the average of our calculated values. We then refitted catchment slope-area data with a fixed (or reference) a_2 value.

4.2. Correlating erosion rate to morphology

We estimated and summarized catchment-averaged erosion rates from cosmogenic radionuclide (CRN) sample analysis (Heimsath et al., 2001; Marshall et al., 2015) from channel sediment in six different small catchments in the central Oregon Coast Range using the CRONUS online calculator (Balco et al., 2008). Each sample integrates erosion rate information from the upstream drainage area, which in our case is less than 10 km^2 for all samples. After erosion rate estimates were calculated, we fit the slope-area data from the corresponding valley networks with Eq. (4) to determine whether the value of a_1 (or the other parameters) can be used to predict erosion rates. To account for the error in each of the CRN-derived erosion rate estimates, we used an inverse-variance weighting scheme. Under the assumption of steady erosion over the integration timescale of the CRN erosion rate estimates, we interpreted these erosion rate data to be a reflection of the long-term uplift rate, although the integration timescale of cosmogenic nuclides in our area is much less than the scale of glacial-interglacial fluctuations.

5. Results

Fitting the empirical model of Stock and Dietrich (2003) to the 83 catchments in our study area resulted in average best-fit parameter values of 0.63 ± 0.081, 15.5 ± 6.4 km^{-2a2}, and 0.73 ± 0.08 for S_0, a_1, and a_2, respectively (Fig. 4A-C). The a_1 distribution is highly dispersed compared to the distributions of S_0 and a_2 as illustrated by a coefficient of variation (ratio of standard deviation to mean) of 0.41 compared to

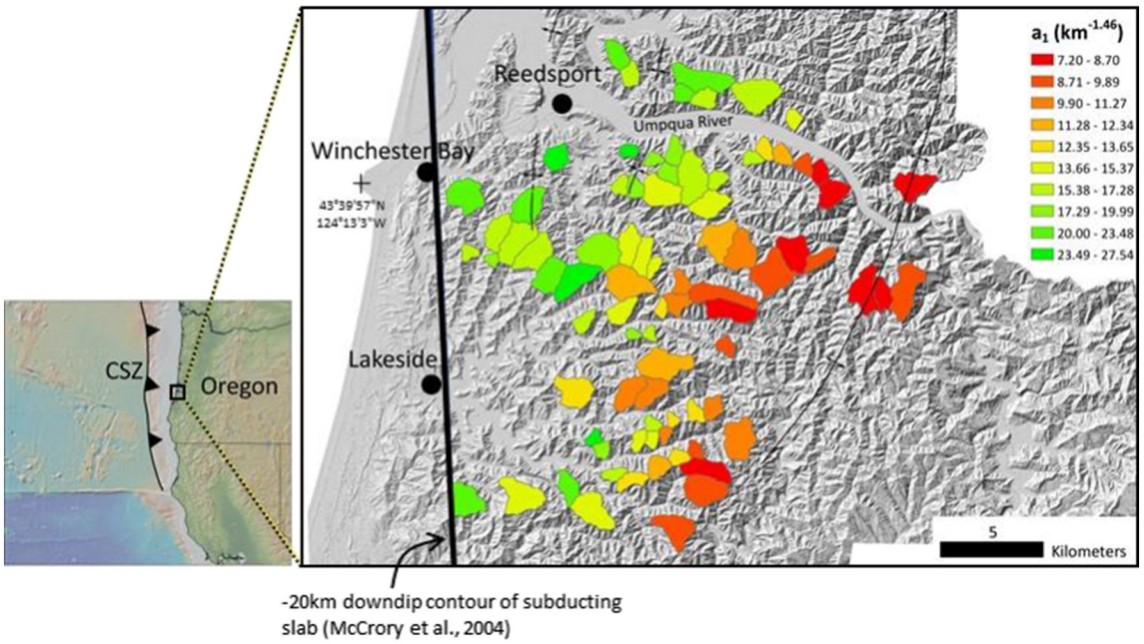

Fig. 3. Regional map and debris flow catchments. Inset map shows regional context of study area atop the Cascadia Subduction Zone (CSZ). Our study catchments are represented by polygons with coloration indicative of the best fitting a_1 value using a fixed a_2 of 0.73. Values of a_1 decrease inland, which reflects a trend of increasing erosion (or uplift) rate. No major faults have been identified in this area, axes of gentle folds are shown. Thick black line is the surface projection of the -20 km downdip contour of the subducting slab from McCrory et al. (2004).

0.13 and 0.11 for S_0 and a_2, respectively. This distribution of a_1, however, contains values with inconsistent units because of the dependence on the corresponding best-fit value of a_2. The relative insensitivity of S_0 agrees with the hypothesis of Stock and Dietrich (2003) that valley slopes at small drainage areas are likely controlled by steep hillslope processes, such as threshold-driven shallow landslides and channel entrainment. Also, the relatively narrow distribution of a_2 values provides empirical support for our use of the reference a_2 approach for estimating dimensionally consistent a_1 values (Fig. 4C). By fixing the reference value of a_2 as 0.73, we refit the empirical slope-area function to all of our study catchments (Figs. 4D-E).

Using the slope-area fits to our six study catchments with cosmogenic nuclide data (Fig. 5; Table 1), we plotted how erosion rate (E, mm/y) varies with a_1 (km$^{-1.46}$) and noted a power-law relationship ($E = \alpha a_1^{\beta}$) with the following best fit parameters, $\alpha = 0.35$ mm/y/km$^{0.5256}$ and $\beta = -0.359$, respectively (Fig. 6). This erosion-morphology transfer function (Fig. 6) implies that we can estimate a_1 values for steepland catchments in our study area (Fig. 3) as a means to map spatial variation in erosion (and uplift under the steady-state assumption).

While S_0 exhibits limited variability amongst our study catchments and a_2 is fixed in order to isolate systematic variations in a_2, our analysis (Fig. 3) shows that a_1 values systematically decrease inland, constituting a systematic increase in erosion rates (from <0.1 to 0.2 mm/y) as one moves eastward and away from -20 km downdip contour of the subducting Juan de Fuca oceanic plate. The relative insensitivity of S_0 to variations in erosion rate may also reflect the influence of nonlinear transport on hillslopes (e.g., Roering, 2008), such that small changes in slope angle can generate large changes in flux. A comprehensive

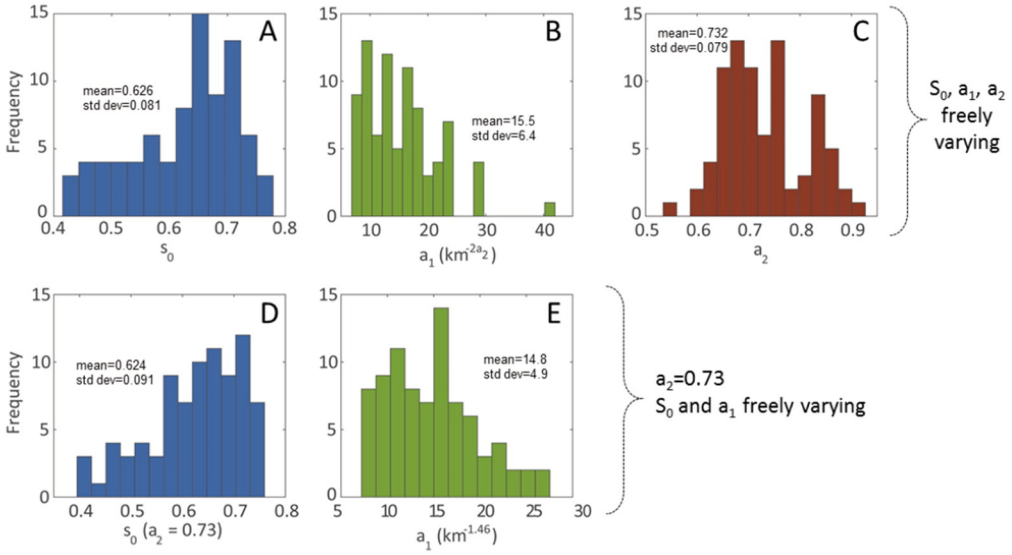

Fig. 4. Parameter distributions. The top row of distributions represents the best fitting parameters (s_0, a_1, and a_2) for 83 catchments in our study area (Fig. 3). The bottom row of distributions represents the best fitting parameters (s_0 and a_1) for models fit with a fixed a_2 of 0.73.

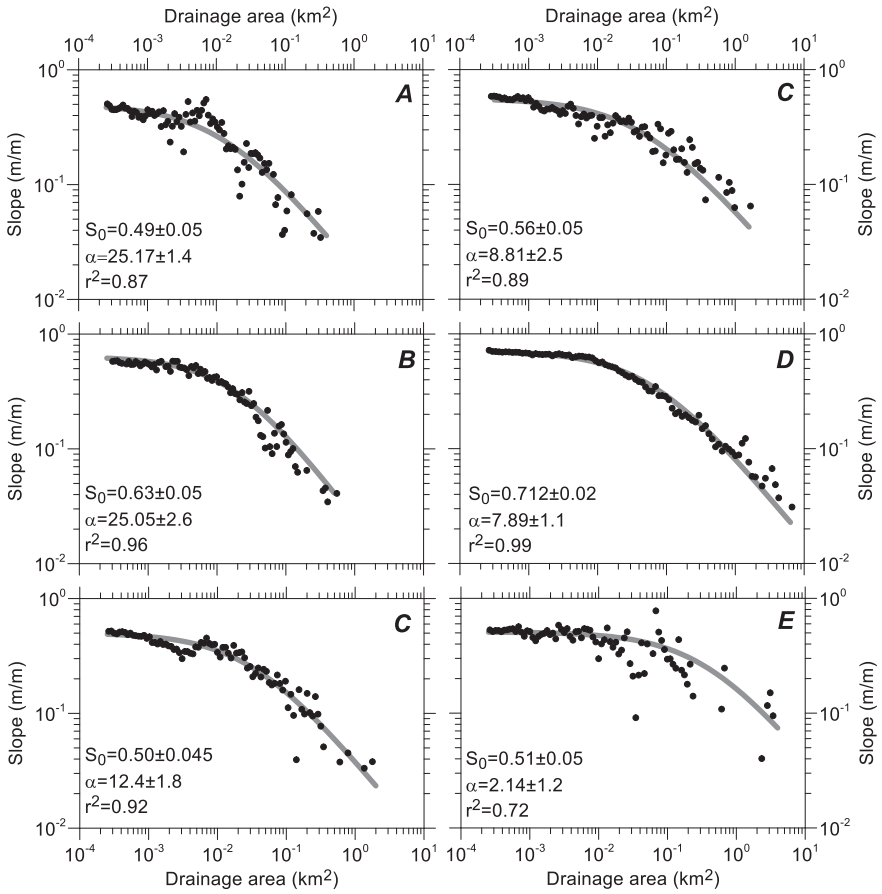

Fig. 5. Catchment slope-area fits. Empirical debris flow model (Eq. 4, thick gray line) fit to binned slope area data for six catchments (black, filled circles) with erosion rate estimates given from cosmogenic nuclides (Table 1). Model parameters and uncertainties are shown given fixed a_2 value of 0.73. Values of a_1 vary systematically with erosion rate and serve as a morphologic proxy for mapping uplift rate assuming steady erosion.

morphologic analysis of systematic variations in hillslope angles and hilltop curvature (e.g., Hurst et al., 2012) in conjunction with the steepland valley network analysis would be illuminating but beyond the scope of this contribution.

6. Application to uplift and earthquake deformation in the Cascadia Subduction Zone

6.1. Background

In the following section, we couple our debris flow network erosion proxy with interseismic uplift and paleoseismology data for the Cascadia Subduction Zone to establish a predictive model for spatial variation in coseismic subsidence typical of megathrust events in Cascadia. This analysis requires the consideration of two disparate timescales of uplift: over hundreds of years, earthquake and post-earthquake strain accumulation and viscoelastic response generate highly transient and discontinuous vertical deformation; whereas over longer timescales, uplift of the margin proceeds because vertical changes associated with the earthquake deformation cycle are not purely elastic as evidenced by the prevalence of marine terraces along central and southern Oregon (Kelsey et al., 1994, 1996). While geomorphologists commonly invoke steady (and uniform) rock uplift to interpret landforms, coseismic and interseismic deformation produce highly variable rock uplift patterns in subduction zone settings (Thatcher, 1984). Despite abundant Native American oral history (Ludwin et al., 2005), there is

Table 1
Cosmogenic radionuclide erosion rates[1]

Sample	Location	Watershed	Concentration (atoms g^{-1} quartz)	Error (atoms g^{-1} quartz)	Erosion rate (mm/y)	Error (mm/y)	Notes
CRN 500	(-123.811°, 43.964°)	Upper Smith River	70902.91 (^{10}Be)	3408.59	0.1023	0.0049	JR, JM
CRN 501	(-124.105°, 43.470°)	Sullivan Creek (North)	53211.86 (^{10}Be)	22369.24	0.124	0.052	JR, JM
CRN 502	(-124.104°, 43.468°)	Sullivan Creek (South)	56073.93 (^{10}Be)	5376.31	0.109	0.011	JR, JM
CRN 503	(-123.905°, 43.670°)	Franklin Creek	44164 (^{10}Be)	2592	0.1559	0.0049	JR, JM
Hads CRN	(-123.824°, 43.985°)	Hadsall Creek	33766.10 (^{10}Be)	4666.26	0.203	0.091	JR, JM
Stream B-R	(-124.113°, 43.469°)	Sullivan Creek (down stream)	287899 (^{26}Al)	89864	0.262	0.081	H2001

[1] The cosmogenic radionuclide-derived erosion rates used to calibrate the functional relationship with a_1 were derived from one published and five unpublished stream sediment samples. ^{10}Be concentrations were obtained for all samples except for the sample from Heimsath et al. (2001), for which ^{26}Al concentration was measured. We used the CRONUS online calculator to calculate catchment-averaged surface erosion rates (Balco et al., 2008). Samples CRN 501 and CRN 502 correspond to nonoverlapping areas of the Sullivan Creek catchment. Sample stream B-R corresponds to a region that overlaps with the regions described by CRN 501 and CRN 502, and a mixing relationship was used to derive the erosion rate for the downstream area corresponding only to sample Stream B-R (Granger et al., 1996). Errors are 1σ propagated from accelerator mass spectrometry (AMS). Notes: JR, JM denotes samples collected by Josh Roering and Jill Marshall and H2001 denotes data from Heimsath et al. (2001).

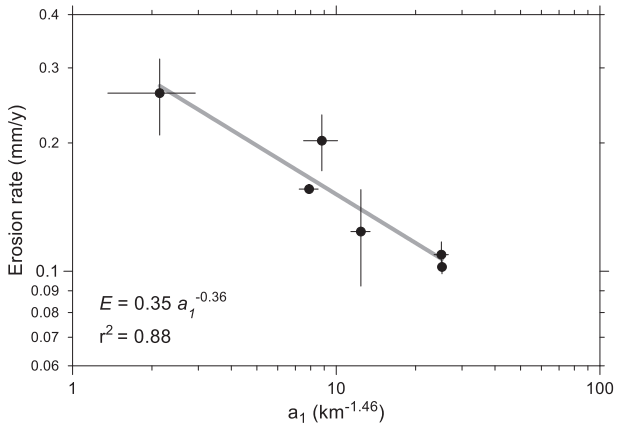

Fig. 6. Erosion-morphology proxy relationship. Erosion rate decreases as a power law function (thick gray line) of a_1 (given fixed value of a_2 equal to 0.73). Error bars reflect two standard errors.

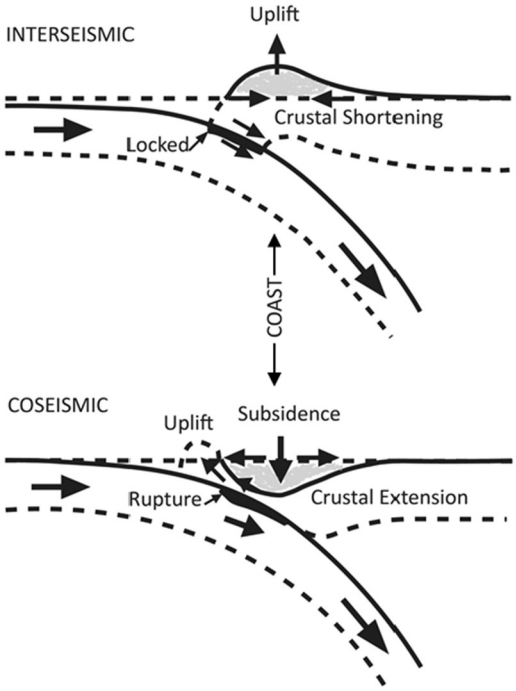

Fig. 7. Subduction zone earthquake deformation cycle. Simplified representation features rapid interseismic uplift in coastal regions as strain accumulates along the locked section of the subduction interface (top). During earthquakes (bottom), strain is released along the interface resulting in uplift near the trench and subsidence in the coastal region.
Modified from Clague (1997).

no instrumental record of a megathrust earthquake in the Pacific Northwest (Atwater and Yamaguchi, 1991; Satake et al., 1996). Historic megathrust events elsewhere highlight the importance of earthquake deformation cycles for determining the evolution of the land surface in these settings (e.g., Tohoku 2011, M_w 9.0; Sumatra 2004, M_w 9.1; Alaska 1964, M_w 9.2; and Chile 1960, M_w 9.5). The dynamic processes that lead to large subduction zone earthquakes are often assumed to be cyclical in nature with coseismic deformation followed by a short period of afterslip and long periods of interseismic deformation that is often assumed to be elastic while the fault zone is locked (Fig. 7; Wang and Tréhu, 2016). Consistent with Kelsey et al. (1994), recent studies imply that a small fraction (~10%) of the deformation experienced during a subduction zone earthquake cycle may be permanent rather than recoverable as implied by purely elastic models (Baker et al., 2013; Wesson et al., 2015).

In Cascadia, geodetic time series (such as leveling, tide gauge, and GPS data) reveal rapid interseismic deformation that exceeds long-term uplift (averaged over a multitude of earthquakes) by more than an order of magnitude (Burgette et al., 2009). Currently, much of the margin experiences rapid interseismic uplift such that megathrust earthquakes generate coseismic subsidence in coastal areas as shown by the abundance of paleoseismology evidence gathered since the 1980s (Atwater, 1987; Witter et al., 2003). Specifically, buried marshes and forests in coastal Washington and Oregon are thought to be reflective of multiple episodes of coseismic subsidence and corresponding tsunamis, which inundated coastal regions and rapidly deposited sediment (Atwater, 1987; Darienzo and Peterson, 1990; Nelson and Personius, 1996). Stratigraphic and microfossil analyses reveal at least 12 events along the central and southern Oregon Coast in the last 6700 years (Witter et al., 2003), which implies a recurrence interval of 570-590 years. Buried soils at Yaquina Bay studied by Graehl et al. (2015) imply a recurrence interval of 420-580 years; while dating of offshore turbidite deposits, believed to have been triggered by coseismic shaking, yield recurrence interval estimates between 500 and 530 years for full-margin rupture events (Goldfinger et al., 2012). These off-shore records also reveal more frequent earthquakes along the Oregon and California coast (Goldfinger et al., 2012) such that the subduction zone may be divided into segments that define the spatial extent of more frequent earthquakes with shorter rupture lengths. Under this assumption, the central Oregon Coast segment may have a recurrence interval of 300 to 380 years (Goldfinger et al., 2012).

Along coastal settings in the Pacific Northwest, sediment cores and outcrops reveal mud-over-peat contacts that correspond to decimeters of nearly instantaneous land-level fall experienced during earthquakes as high tidal marshes or swamps dropped and subsequently buried by intertidal sediments (and sometimes tsunamites). The sedimentary signature of interseismic uplift is the accumulation of muddy sediments capped by peat. Coastal coseismic subsidence estimates for the 26 January 1700 Cascadia earthquake range from 0.3 to >1.0 m, and areas of negligible subsidence are proposed to reflect heterogeneous surface rupture and potentially fault segmentation (Leonard et al., 2010; Milker et al., 2016). The inland extent of coseismic subsidence, however, which likely depends on the downdip rupture pattern and slip distribution, remains poorly constrained and is not readily derived from geodetic data sets.

6.2. Estimating uplift and coseismic subsidence

Slope-area data for steep, low-order catchments in our study area imply that long-term uplift rates increase inland (Fig. 3); and in order to connect our analysis to subduction zone earthquakes, we use the -20 km downdip contour of the down-going slab (defined by McCrory et al., 2004) as a reference for defining spatial trends in long-term erosion/uplift, interseismic uplift, and coseismic subsidence. For simplicity, we approximate the plate interface as fully locked, consistent with numerous lines of evidence (Wang and Tréhu, 2016). We also assume megathrust earthquakes to be periodic, although variable recurrence intervals are easily implemented with our methodology. Furthermore, given the consistency of plate convergence over geologic timescales, we assume that interseismic uplift rates are relatively constant between earthquake cycles. Although afterslip can manifest as a short-lived deviation from constant interseismic uplift following earthquakes (Thatcher, 1984; Wang et al., 2012), we neglect its potential time-dependent influence on the uplift field in order to simplify our analysis. Given these assumptions, the total surface uplift accumulated during one interseismic period (Δz_i) is given as $\Delta z_i = IR$, where I represents interseismic uplift rate (mm/y) and R is the average earthquake recurrence interval (y). Recognizing that inelastic vertical strain (via sediment underplating, buoyancy, or another factor) contributes to

permanent uplift of the coastal ranges, we can similarly calculate the amount of permanent (or long-term) uplift (Δz_L) that accumulates over one earthquake cycle as $\Delta z_L = UR$, where U is long-term uplift rate. Subtracting Δz_L from Δz_i gives the coseismic subsidence (S, mm) for a subduction zone earthquake as

$$S = R(I\text{-}U) \quad (5)$$

which can be calculated at any location along or inland of the margin.

Interseismic uplift rates obtained from leveling and tidal gauge records (Kelsey et al., 1994; Burgette et al., 2009) to investigate the pattern of locking along the Cascadia Subduction Zone plate interface show along-strike (N-S) variation that remains to be explained. Thus, we focused on the central Oregon Coast segment as characterized by Burgette et al. (2009); Fig. 8A). This data set coincides with our study catchments, enabling us to couple east-west variations in interseismic uplift with long-term uplift using Eq. (5). We plotted interseismic uplift rate, as well as long-term uplift rate estimates from our proposed morphology-erosion proxy (Fig. 8B), with distance from surface projection of the -20 km downdip contour of the subducting slab. Rates of interseismic uplift are highest near the coast (~4 mm/y) and decline rapidly in the landward direction over a distance of ~60 km (Fig. 8A). As shown in Fig. 8B, our long-term uplift rates established from debris flow catchments span 25 km of the Burgette et al. (2009) data set and reveal the opposite trend: long-term uplift is low near the coast and increases linearly in the landward direction. To solve Eq. (5) along our east-west transect, we fit the interseismic data with a stiff spline function and the long-term data with a linear function (Fig. 8Bii) using an inverse-variance weighting scheme.

We use Eq. (5) to generate predictions of coseismic subsidence for earthquake recurrence intervals of 300 and 500 years (Fig. 8Biii). In each scenario, coseismic subsidence is highest near the coast and decreases inland, consistent with the predictions of Hyndman and Wang (1995) and Dragert et al. (1994). Our coseismic subsidence predictions for estuaries and marshes along this section of the central Oregon coast are 0.42 ± 0.06 m and 0.70 ± 0.10 m (mean with 95% CI) for recurrence intervals of 300 and 500 years, respectively. These coastal subsidence values coincide with those inferred from the A.D. 1700 event as well as previous Cascadia megathrust earthquakes (Witter et al., 2003; Leonard et al., 2010; Milker et al., 2016). Our model also predicts that coseismic subsidence decreases to ~0.2 m (or less) at 25 km east of the -20 km contour and likely decays to negligible values within 50-60 km (Fig. 8Biii). This zone of rapidly declining coseismic subsidence is consistent with the modeled downdip rupture width (measured east-west) for the A.D. 1700 event (Wang et al., 2013; Wang and Tréhu, 2016), although rupture length is likely complex owing to the ambiguous transition from a fully locked to freely slipping interface farther down the interface.

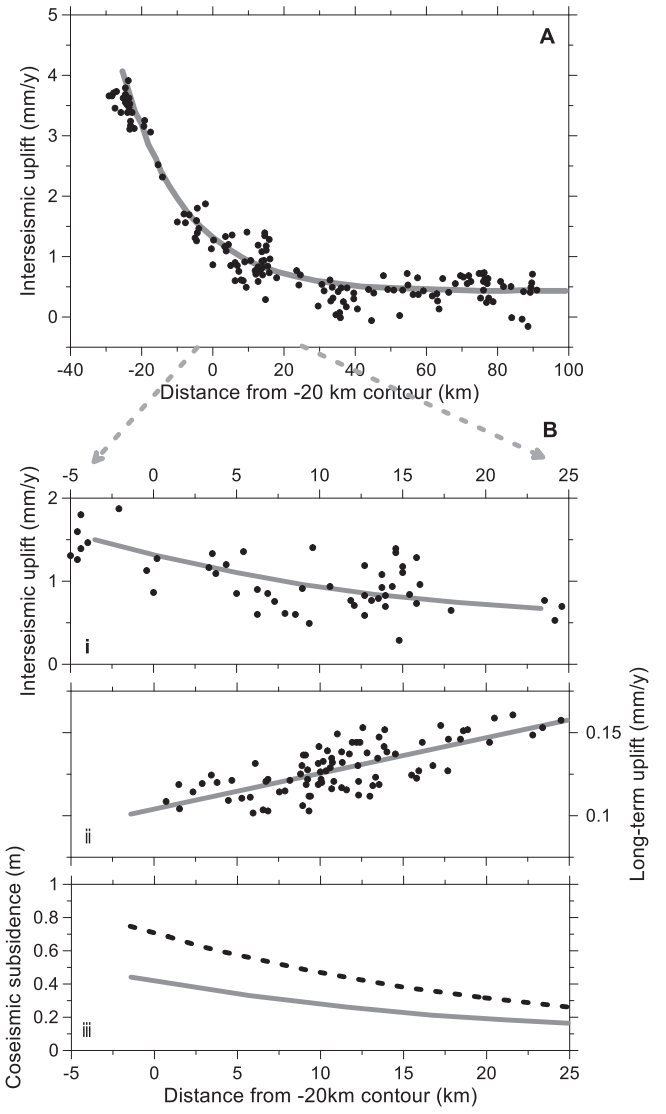

Fig. 8. Uplift and subsidence transect. (A) Interseismic uplift rates plotted with distance from the -20 km contour. Black dots represent leveling measurements, with the gray line a stiff spline fit to the central coast data from Burgette et al. (2009). **(B)** (i) A subset of interseismic uplift data (from Fig. 8A). (ii) Long-term erosion (or uplift) rate plotted with distance from the -20 km contour. Black dots represent the raw values obtained using the erosion rate function from Figure 6 and assuming erosion balances uplift. (iii) Coseismic subsidence estimates (Eq. 5) using the trends from (A) and (B) and subduction earthquake recurrence intervals of 300 (blue) and 500 (red) years, respectively.

7. Discussion

By developing a method to extract information on local base level from the longitudinal profiles of steepland headwater catchments, a large portion of the landscape that is often eschewed can be exploited to make inferences on patterns of uplift rate and lithologic and climate variations. Debris flow valley profiles have the potential to reveal long-term uplift rates over 10^4 year timescales and are abundant throughout most tectonically active areas lacking significant glaciation. Our assumption of steady state (erosion balances rock uplift) is predicated on the notion that the morphologic patterns we observe result from the integration of landscape evolution accomplished over numerous climate intervals (such as interglacial-glacial cycles) rather than reflect the signature of transient adjustment. In this region, erosion rates for timescales exceeding those achieved with cosmogenic nuclides are lacking as thermochronology findings have proven to be ambiguous (e.g., Batt et al., 2002).

7.1. Morphologic signature of debris flow processes

Our morphologic erosion rate proxy represents curvature of slope-area data (defined by a_1) as originally proposed by Stock and Dietrich (2003), and the application to our study catchments confirms that the other two parameters (a_2 and S_0) exhibit minimal variance (Fig. 4). Our observation that a_1 varies with erosion rate supports the notion that hillslope angles are relatively insensitive to erosion rate, whereas downstream fluvial reaches track erosion (Ouimet et al., 2009; DiBiase et al., 2010). To determine whether our choice of a reference concavity value (a_2) influences our results, we conducted a sensitivity analysis by fitting several versions of the empirical slope-area function with extreme fixed a_2 values. Because a_2 ranges from 0.5 to 0.9 in our study group, we repeated our reference a_2 analysis using fixed values of 0.5 and 0.9 to test whether the spatial pattern of long-term uplift rate estimates change. The resulting a_1 values exhibited very similar patterns

and our predicted erosion rates were unaffected, confirming the robustness of the reference a_2 approach. Nonetheless, the generality of our parameter estimates is unclear and we anticipate that climate and lithologic factors modulate process-form feedbacks. Importantly, the empirical model used here should not be confused with a process-based formulation (Dietrich et al., 2003) but rather serves as a convenient functional form whose parameters may be indirectly related to geomorphic process models.

Our analysis of debris flow valleys considers only the upper most portion of the valley network where debris flows traverse and scour the valley floor. These slopes typically coincide with a scaling transition in slope and drainage area and are occupied by reaches where debris flow runouts and long-term fluvial features are observed (Stock and Dietrich, 2003). While previous studies proposed multiple power law scaling regimes (Lague and Davy, 2003; DiBiase et al., 2012), here we demonstrate that western Oregon watersheds exhibit a continuous (or curved) deviation from power law scaling rather than a discrete scaling break (Stock and Dietrich, 2003). Airborne LiDAR data sets are key for defining valley network form, although field observations will prove crucial for delineating the extent of fluvial and debris flow (or sometimes termed colluvial) regimes in valley networks (Stock and Dietrich, 2006; DiBiase et al., 2012).

Different means of debris flow initiation may contribute to varying morphologic signatures. Densely vegetated unchanneled valleys of the Pacific Northwest favor initiation via shallow landslides at discrete locations in the network (Dietrich and Dunne, 1978). By contrast, more arid settings, such as the San Gabriel Mountains, exhibit debris flows prompted by dispersed entrainment of unconsolidated colluvium in steep valley bottoms (Prancevic et al., 2014). The drainage network scale implications of these different mechanisms, however, remains unexplored. A theoretical (and parameter-rich) model for debris flow incision proposed by Stock and Dietrich (2006) stated that the transition in slope-area scaling arises because of the tendency for valley slope to adjust to the long-term frequency and efficacy of debris flow passage. Their model generates curved slope-area relationships owing to the following effects: (i) incision rate *increases* downvalley because (a) the increased frequency of debris flow events given that source areas increase with drainage area, and 9b) the increasing length of debris flows via colluvial entrainment; and (ii) incision rates *decreases* downvalley resulting from (a) decreases in inertial normal stress at lower slope angles and (b) exposure of progressively stronger, less-weathered bedrock in valley bottoms (Stock and Dietrich, 2006). The combined influence of these processes and variables results in a morphologic signature consistent with the empirical model that we adopt here.

7.2. Uplift and the earthquake deformation cycle

The east-west long-term uplift trend that we observe is statistically significant, although suitable coastal catchments are relatively sparse owing to the increasing density of wide valley bottoms influenced by sea-level rise during highstands. Additionally, marine terrace remnants near the coast can disrupt the uniform valley-ridge morphology that is typical of inland catchments and reflect transient conditions. Meanwhile, the inland extent of our study region is limited by the current availability of high-resolution LiDAR data although the Oregon Department of Geology and Mineral Industries (DOGAMI) is currently acquiring data for the region. Thus, the eastern limit of LiDAR coverage currently precludes our estimates of long-term uplift rates from extending inland more than 25 km from the -20 km downdip contour of McCrory et al. (2004).

Furthermore, the ~43.5° latitude of our transect corresponds with a proposed segment boundary along the Cascadia Subduction Zone marked by the landward continuation of the Blanco Fracture Zone (Porrit et al., 2011). Although some studies infer a structural transition (and thereby imply a unique earthquake regime) at this latitude, observations for the Gorda and Juan de Fuca plates do not exhibit systematic variations in seismic velocity with topography or tremor (Porrit et al., 2011). This finding also contradicts the hypothesis that topography in the coastal ranges developed via buoyancy and thermal effects and instead implicates sediment underplating as a more likely source of permanent uplift of the coastal ranges (Pavlis and Bruhn, 1983; Personius, 1995). Finally, the interseismic uplift field we use in this analysis is consistent with other profiles north of our study area, situated atop the Siletzia block (Burgette et al., 2009), supporting the regional relevance of our study area and results.

Defining the gradient of long-term uplift across coastal ranges like our western Oregon study area also invites examination of sea level fluctuations. For a catchment that subsides during a subduction zone earthquake, relative sea level rises and raises the local base level, possibly inundating previously incised valley floors. This would inhibit the ability of valley-forming processes to incise until interseismic uplift accumulates to a sufficient level. As a result, the uplift (and erosion) gradient that we infer perpendicular to the coast may be directly modulated by the proportion of the earthquake cycle during which valley bottoms and outlets are inundated and thus insulated from incision. Despite evidence indicating that the Oregon Coast Range has been experiencing long-term uplift since the Miocene, our results indicate that the rate of long-term uplift changes over relatively short distances in the absence of identifiable structures (Kelsey et al., 1996). Furthermore, interseismic uplift rates tend to change rapidly near the coast, indicating a significant gradient in strain accumulation along the subduction interface (Fig. 9). Further inland, interseismic uplift rates appear to approach long-term rates, implying minimal surface elevation change during megathrust earthquakes in the eastern portion of the coastal ranges and the Willamette Valley (Fig. 9).

We compared our estimates of coseismic subsidence with previous measurements established from buried soils. Leonard et al. (2004, 2010) aggregated several estimates of coastal coseismic subsidence of buried marshes and found that coseismic subsidence ranged from 0 to 2 m along Cascadia. For marshes and estuaries that overlap with our study area, coseismic subsidence estimates are 0.46 $\pm$ 0.31 and 0.61 $\pm$ 0.32 m, respectively (Peterson and Darienzo, 1989; Darienzo and Peterson, 1990; Nelson et al., 1996, 1998). Our estimates of coseismic subsidence between zero and the -20 km contour, which approximates the coastline depending on latitude, are in agreement with these observed values. This correspondence occurs despite our adoption of several assumptions that simplify subduction earthquake dynamics. For example, Wang et al. (2012) provided a detailed description of the subduction earthquake cycle, where afterslip along the fault as well as viscoelastic relaxation of the mantle occur prior to relocking. Because a megathrust event and/or cycle has never been documented in Cascadia, it is difficult to determine spatial and temporal controls on coastal uplift. Based on historic megathrust events from other subduction zones, afterslip (or post-seismic slip) is believed to occur over timescales of months to years post-earthquake with fault locking occurring over the vast majority of the interseismic period (Wang et al., 2012). The interseismic uplift rates of Burgette et al. (2009) represented several decades of the current >300-year interseismic period, yet we assume these rates to be relevant over longer timescales as well as during other interseismic periods (Thatcher, 1984). While slip downdip of the locked segment of the plate interface may be relatively consistent over time, this does not imply that coseismic and interseismic uplift exhibit characteristic behavior (Clague, 1997).

Our adoption of a characteristic earthquake model to predict coseismic subsidence does not contradict the well-studied earthquake history in the region (Atwater and Hemphill-Haley, 1997; Witter et al., 2003; Goldfinger et al., 2012). Rather, our subsidence model can readily be modified to explore what different recurrence intervals and uplift patterns imply about coseismic subsidence. The inland extension of coseismic subsidence has been difficult to estimate because of sparse and poorly preserved stratigraphic records. Our predictions provide a

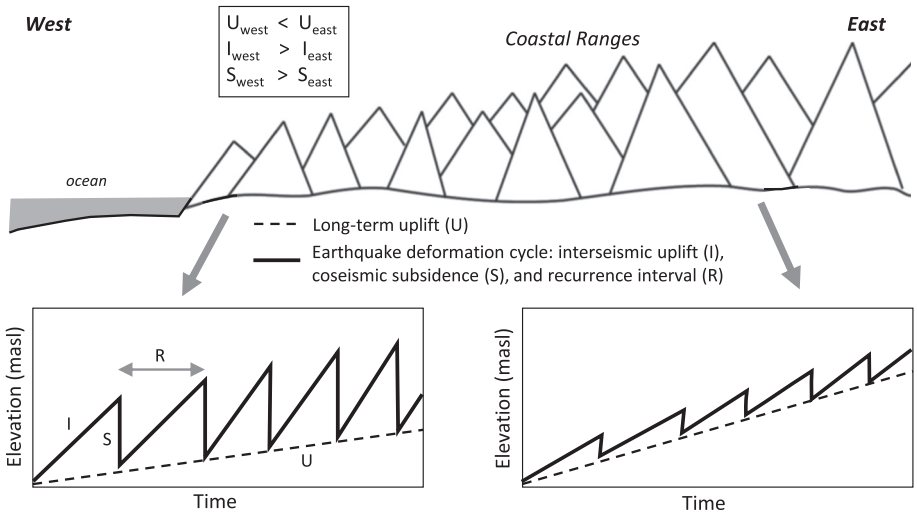

Fig. 9. Uplift and subduction zone earthquake deformation cycle. Schematic diagram of interseismic uplift (*I*) and coseismic subsidence (*S*) for two locations (one coastal and one inland) along a margin-perpendicular (or east-west) transect across the central Oregon Coast Range. Sawtooth time-series plots show reference bedrock (or surface) elevation change over the interseismic interval as solid lines and permanent uplift are shown by the black long-dashed line. Near the coast, interseismic uplift rates are high but long-term rates are low, indicating the dominant role of earthquake deformation on uplift. Inland, interseismic uplift is lower and long-term uplift is higher, resulting in minimal coseismic subsidence and decreased importance of earthquakes in vertical surface elevation changes.

simple, yet testable framework for reconciling tectonic deformation across highly diverse timescales.

8. Conclusions

Debris flow networks are ubiquitous and localized in mountainous settings, yet they have not been exploited to extract constraints on uplift and erosion. By adopting a previously proposed empirical function to characterize the curvature of slope-area data for debris flow networks, we show that the model parameters vary systematically in our central Oregon Coast Range study area. Consistent with the predictions of Stock and Dietrich (2003), the transition between hillslope and fluvial process regimes becomes sharper with increasing uplift rate, causing steep debris flow reaches to extend farther downstream in higher uplifting sites than slower ones. A power-law relationship between the parameter that describes this transition and erosion rate determined from cosmogenic nuclides enables us to map erosion (and uplift) for an east-west transect. Our results show increasing long-term uplift eastward that contrasts with interseismic uplift rates that decrease inland. We used a simple representation of the earthquake deformation cycle to couple these long-term and interseismic uplift estimates with Holocene earthquake recurrence interval estimates to predict the magnitude of coseismic subsidence. Our calculations generate subsidence values of 0.4 to 0.7 m near the coast, consistent with stratigraphic information, and show that subsidence (and the effect of earthquakes on vertical deformation) decreases inland over more than 25 km, which may reflect the downdip extent of the locked zone of the subduction zone interface.

Acknowledgements

The authors thank Colin Pain, two anonymous reviewers, and Editor R. Marston for their valuable input during the review process. JJR was supported by NSF EAR-1420898. The channel-smoothing code was generously provided by Scott Miller. The authors thank Ian Madin and staff of Oregon Department of Geology and Mineral Industries (DOGAMI) for LiDAR acquisition. The authors thank David Furbish, Rina Schumer, Harvey Kelsey, Rebecca Bendick, Scott McCoy, and John Stock for inspiration and helpful discussions.

References

Ahnert, F., 1970. Functional relationships between denudation, relief, and uplift in large, mid-latitude drainage basins. Am. J. Sci. 268, 243–263.
Almond, P., Roering, J., Hales, T., 2007. Using soil residence time to delineate spatial and temporal patterns of transient landscape response. Earth Surface, Journal of Geophysical Research http://dx.doi.org/10.1029/2006JF000568.
Attal, M., Cowie, P.A., Whittaker, A.C., Hobley, D., Tucker, G.E., Roberts, G.P., 2011. Testing fluvial erosion models using the transient response of bedrock rivers to tectonic forcing in the Apennines, Italy. J. Geophys. Res. Earth Surf. http://dx.doi.org/10.1029/2010JF001875.
Atwater, B.F., 1987. Evidence for great Holocene earthquakes along the outer coast of Washington State. Science 236, 942–944.
Atwater, B.F., Hemphill-Haley, E., 1997. Recurrence intervals for great earthquakes of the past 3,500 years at northeastern Willapa Bay, Washington. USGS Professional Paper 1576 (108 pp.).
Atwater, B.F., Yamaguchi, D.K., 1991. Sudden, probably coseismic submergence of Holocene trees and grass in coastal Washington State. Geology 19, 706–709.
Audet, P., Bostock, M.G., Boyarko, D.C., Brudzinski, M.R., Allen, R.M., 2010. Slab morphology in the Cascadia fore arc and its relation to episodic tremor and slip. J. Geophys. Res. 115, B00A16. http://dx.doi.org/10.1029/2008JB006053.
Baker, A., Allmendinger, R.W., Owen, L.A., Rech, J.A., 2013. Permanent deformation caused by subduction earthquakes in northern Chile. Nat. Geosci. 6 (6), 492–496.
Balco, G., Stone, J.O., Lifton, N.A., Dunai, T.J., 2008. A complete and easily accessible means of calculating surface exposure ages or erosion rates from 10 Be and 26 Al measurements. Quat. Geochronol. 3, 174–195.
Baldwin, E.M., 1956, Geologic map of the lower Siuslaw River Area, Oregon: U.S. Geological Survey Oil and Gas Investigations Map OM-186, 1 sheet, scale 1:62,500.
Batt, G.E., Brandon, M.T., Farley, K., Gosse, J.C., 2002. Uplift and erosion of the Cascadia Forearc High as indicated by (U-Th)/He apatite dating. Annual Geological Society of America Abstracts and Program.
Benda, L., 1990. The influence of debris flows on channels and valley floors in the Oregon Coast Range, USA. Earth Surf. Process. Landf. 15, 457–466.
Benda, L., Dunne, T., 1997. Stochastic forcing of sediment supply to channel networks from landsliding and debris flow. Water Resour. Res. 33, 2849–2863.
Beschta, R.L., 1978. Long-term patterns of sediment production following road construction and logging in the Oregon Coast Range. Water Resour. Res. 14, 1011–1016.
Bierman, P., Clapp, E., Nichols, K., Gillespie, A., Caffee, M.W., 2001. Using cosmogenic nuclide measurements in sediments to understand background rates of erosion and sediment transport. Landscape Erosion and Evolution Modeling. Springer, pp. 89–115.
Binnie, S.A., Phillips, W.M., Summerfield, M.A., Fifield, L.K., 2007. Tectonic uplift, threshold hillslopes, and denudation rates in a developing mountain range. Geology 35, 743–746.
Burgette, R.J., Weldon, R.J., Schmidt, D.A., 2009. Interseismic uplift rates for western Oregon and along-strike variation in locking on the Cascadia subduction zone. J. Geophys. Res. http://dx.doi.org/10.1029/2008JB005679.
Chatanantavet, P., Parker, G., 2009. Physically based modeling of bedrock incision by abrasion, plucking, and macroabrasion. J. Geophys. Res. Earth Surf. http://dx.doi.org/10.1029/2008JF001044.
Clague, J.J., 1997. Evidence for large earthquakes at the Cascadia subduction zone. Rev. Geophys. 35, 439–460.

Crosby, B.T., Whipple, K.X., 2006. Knickpoint initiation and distribution within fluvial networks: 236 waterfalls in the Waipaoa River, North Island, New Zealand. Geomorphology 82 (1), 16–38.
Cyr, A.J., Granger, D.E., Olivetti, V., Molin, P., 2010. Quantifying rock uplift rates using channel steepness and cosmogenic nuclide–determined erosion rates: Examples from northern and southern Italy. Lithosphere 2, 188–198.
Darienzo, M.E., Peterson, C.D., 1990. Episodic tectonic subsidence of late Holocene salt marshes, northern Oregon central Cascadia margin. Tectonics 9, 1–22.
DiBiase, R.A., Whipple, K.X., Heimsath, A.M., Ouimet, W.B., 2010. Landscape form and millennial erosion rates in the San Gabriel Mountains, CA. Earth Planet. Sci. Lett. 289, 134–144.
DiBiase, R.A., Heimsath, A.M., Whipple, K.X., 2012. Hillslope response to tectonic forcing in threshold landscapes. Earth Surf. Process. Landf. 37:855–865. http://dx.doi.org/10.1002/esp.3205.
Dietrich, W., Dunne, T., 1978. Sediment budget for a small catchment in a mountainous terrain. Z. Geomorphol. Suppl. 29, 191–206.
Dietrich, W.E., Bellugi, D.G., Sklar, L.S., Stock, J.D., Heimsath, A.M., Roering, J.J., 2003. Geomorphic transport laws for predicting landscape form and dynamics. Predict. Geomorphol. 103–132.
Dragert, H., Hyndman, R., Rogers, G., Wang, K., 1994. Current deformation and the width of the seismogenic zone of the northern Cascadia subduction thrust. J. Geophys. Res. Solid Earth 99, 653–668.
Duvall, A., Kirby, E., Burbank, D., 2004. Tectonic and lithologic controls on bedrock channel profiles and processes in coastal California. J. Geophys. Res. Earth Surf. http://dx.doi.org/10.1029/2003JF000086.
Fernandes, N.F., Dietrich, W.E., 1997. Hillslope evolution by diffusive processes: The timescale for equilibrium adjustments. Water Resour. Res. 33 (6), 1307–1318.
Finnegan, N.J., Sklar, L.S., Fuller, T.K., 2007. Interplay of sediment supply, river incision, and channel morphology revealed by the transient evolution of an experimental bedrock channel. J. Geophys. Res. Earth Surf. http://dx.doi.org/10.1029/2006JF000569.
Finnegan, N.J., Schumer, R., Finnegan, S., 2014. A signature of transience in bedrock river incision rates over timescales of 104-107 years. Nature 505 (7483), 391–394.
Flint, J., 1974. Stream gradient as a function of order, magnitude, and discharge. Water Resour. Res. 10, 969–973.
Gallen, S.F., Pazzaglia, F.J., Wegmann, K.W., Pederson, J.L., Gardner, T.W., 2015. The dynamic reference frame of rivers and apparent transience in incision rates. Geology 43 (7), 623–626.
Gasparini, N.M., Brandon, M.T., 2011. A generalized power law approximation for fluvial incision of bedrock channels. J. Geophys. Res. Earth Surf. 116 (F2). http://dx.doi.org/10.1029/2009JF001655.
Geological Survey, U.S., 2006. Quaternary fault and fold database for the United States. (USGS web site: http//earthquakes.usgs.gov/regional/qfaults/).
Goldfinger, C., Nelson, C.H., Morey, A.E., Joel, E.J., Patton, J., Karabanov, E., Gutierrez-Pastor, J., Eriksson, A., Gracia, E., Dunhill, G., Enkin, R., Dallimore, A., Valiier, T., 2012. Turbidite Event History — Methods and Implications for Holocene Paleoseismicity of the Cascadia Subduction Zone. U.S. Geological Survey Professional Paper 1661-F (170 pp.-170 pp.).
Graehl, N.A., Kelsey, H.M., Witter, R.C., Hemphill-Haley, E., Engelhart, S.E., 2015. Stratigraphic and microfossil evidence for a 4500-year history of Cascadia subduction zone earthquakes and tsunamis at Yaquina River estuary, Oregon, USA. Geol. Soc. Am. Bull. 127, 211–226.
Granger, D.E., Kirchner, J.W., Finkel, R., 1996. Spatially averaged long-term erosion rates measured from in situ-produced cosmogenic nuclides in alluvial sediment. The Journal of Geology 249–257.
Hack, J.T., 1973. Stream-profile analysis and stream-gradient index. J. Res. US Geol. Survey 1, 421–429.
Harel, M.A., Mudd, S.M., Attal, M., 2016. Global analysis of the stream power law parameters based on worldwide 10 Be denudation rates. Geomorphology 268, 184–196.
Harkins, N., Kirby, E., Heimsath, A., Robinson, R., Reiser, U., 2007. Transient fluvial incision in the headwaters of the Yellow River, northeastern Tibet, China. J. Geophys. Res. Earth Surf. http://dx.doi.org/10.1029/2006JF000570.
Heimsath, A.M., Dietrich, W.E., Nishiizumi, K., Finkel, R.C., 2001. Stochastic processes of soil production and transport: Erosion rates, topographic variation and cosmogenic nuclides in the Oregon Coast Range. Earth Surf. Process. Landf. 26, 531–552.
Heller, P.L., Dickinson, W.R., 1985. Submarine ramp facies model for delta-fed, sand-rich turbidite systems. AAPG Bull. 69, 960–976.
Hobley, D.E., Sinclair, H.D., Mudd, S.M., Cowie, P.A., 2011. Field calibration of sediment flux dependent river incision. J. Geophys. Res. Earth Surf. http://dx.doi.org/10.1029/2010JF001935.
Howard, A.D., 1997. Badland morphology and evolution: Interpretation using a simulation model. Earth Surf. Process. Landf. 22, 211–227.
Howard, A.D., Kerby, G., 1983. Channel changes in badlands. Geol. Soc. Am. Bull. 94, 739–752.
Hsu, L., Dietrich, W.E., Sklar, L.S., 2008. Experimental study of bedrock erosion by granular flows. J. Geophys. Res. Earth Surf. http://dx.doi.org/10.1029/2007JF000778.
Hurst, M.D., Mudd, S.M., Walcott, R., Attal, M., Yoo, K., 2012. Using hilltop curvature to derive the spatial distribution of erosion rates. J. Geophys. Res. Earth Surf. http://dx.doi.org/10.1029/2011JF002057.
Hurtrez, J.E., Sol, C., Lucazeau, F., 1999. Effect of drainage area on hypsometry from an analysis of small-scale drainage basins in the Siwalik Hills (Central Nepal). Earth Surf. Process. Landf. 24, 799–808.
Hyndman, R., Wang, K., 1995. The rupture zone of Cascadia great earthquakes from current deformation and the thermal regime. J. Geophys. Res. Solid Earth 100, 22133–22154.
Kean, J.W., McCoy, S.W., Tucker, G., Staley, D.M., Coe, J.A., 2013. Runoff-generated debris flows: Observations and modeling of surge initiation, magnitude, and frequency. J. Geophys. Res. http://dx.doi.org/10.1002/jgrf.20148.
Kelsey, H.M., Engebretson, D.C., Mitchell, C.E., Ticknor, R.L., 1994. Topographic form of the Coast Ranges of the Cascadia margin in relation to coastal uplift rates and plate subduction. J. Geophys. Res. Solid Earth 99 (B6), 12245–12255.
Kelsey, H.M., Ticknor, R.L., Bockheim, J.G., Mitchell, E., 1996. Quaternary upper plate deformation in coastal Oregon. Geol. Soc. Am. Bull. 108, 843–860.
Kirby, E., Whipple, K., 2001. Quantifying differential rock-uplift rates via stream profile analysis. Geology 29, 415–418.
Kirby, E., Whipple, K.X., 2012. Expression of active tectonics in erosional landscapes. J. Struct. Geol. 44, 54–75.
Lague, D., 2014. The stream power river incision model: evidence, theory and beyond. Earth Surf. Process. Landf. 39 (1), 38–61.
Lague, D., Davy, P., 2003. Constraints on the long-term colluvial erosion law by analyzing slope-area relationships at various tectonic uplift rates in the Siwaliks Hills (Nepal). J. Geophys. Res. http://dx.doi.org/10.1029/2002JB001893.
Lague, D., Davy, P., Crave, A., 2000. Estimating uplift rate and erodibility from the area-slope relationship: Examples from Brittany (France) and numerical modelling. Phys. Chem. Earth Solid Earth Geod. 25, 543–548.
Lavé, J., Burbank, D., 2004. Denudation processes and rates in the Transverse Ranges, southern California: Erosional response of a transitional landscape to external and anthropogenic forcing. J. Geophys. Res. Earth Surf. http://dx.doi.org/10.1029/2003JF000023.
Leonard, L.J., Hyndman, R.D., Mazzotti, S., 2004. Coseismic subsidence in the 1700 great Cascadia earthquake: Coastal estimates versus elastic dislocation models. Geol. Soc. Am. Bull. 116, 655–670.
Leonard, L.J., Currie, C.A., Mazzotti, S., Hyndman, R.D., 2010. Rupture area and displacement of past Cascadia great earthquakes from coastal coseismic subsidence. Geol. Soc. Am. Bull. 122 (11-12), 2079–2096.
Ludwin, R.S., Dennis, R., Carver, D., McMillan, A.D., Losey, R., Clague, J., Jonientz-Trisler, C., Bowechop, J., Wray, J., James, K., 2005. Dating the 1700 Cascadia earthquake: Great coastal earthquakes in native stories. Seismol. Res. Lett. 76 (2), 140–148.
Mackin, J.H., 1948. Concept of the graded river. Geol. Soc. Am. Bull. 59, 463–512.
Marshall, J.A., Roering, J.J., 2014. Diagenetic variation in the Oregon Coast Range: Implications for rock strength, soil production, hillslope form, and landscape evolution. J. Geophys. Res. http://dx.doi.org/10.1002/2013JF003004.
Marshall, J.A., Roering, J.J., Bartlein, P.J., Gavin, D.G., Granger, D.E., Rempel, A.W., Praskievicz, S.J., Hales, T.C., 2015. Frost for the trees: Did climate increase erosion in unglaciated landscapes during the late Pleistocene? Sci. Adv. 1 (10), 1500715.
McCoy, S.W., Kean, J.W., Coe, J.A., Tucker, G.E., Staley, D.M., Wasklewicz, T.A., 2012. In situ measurements of sediment entrainment from the headwaters of a steep catchment. J. Geophys. Res. http://dx.doi.org/10.1029/2011JF002278.
McCrory, P.A., Blair, J.L., Oppenheimer, D.H., Walter, S.R., 2004. Depth to the Juan de Fuca slab beneath the Cascadia subduction margin: A 3-D model for sorting earthquakes. US Department of the Interior, US Geological Survey, Data Series 91 (version 1.2).
McNeill, L.C., Goldfinger, C., Kulm, L.D., Yeats, R.S., 2000. Tectonics of the Neogene Cascadia forearc basin: Investigations of a deformed late Miocene unconformity. Geol. Soc. Am. Bull. 112, 1209–1224.
Milker, Y., Nelson, A.R., Horton, B.P., Engelhart, S.E., Bradley, L.A., Witter, R.C., 2016. Differences in coastal subsidence in southern Oregon (USA) during at least six prehistoric megathrust earthquakes. Quat. Sci. Rev. 142, 143–163.
Milliman, J.D., Syvitski, J.P., 1992. Geomorphic/tectonic control of sediment discharge to the ocean: the importance of small mountainous rivers. J. Geol. 525–544.
Montgomery, D.R., Buffington, J.M., 1997. Channel-reach morphology in mountain drainage basins. Geol. Soc. Am. Bull. 109, 596–611.
Mudd, S.M., 2016. Detection of transience in eroding landscapes. Earth Surf. Process. Landf. http://dx.doi.org/10.1002/esp.3923.
Nelson, A.R., Personius, S.F., 1996. Great-earthquake potential in Oregon and Washington—An overview of recent coastal geologic studies and their bearing on segmentation of Holocene ruptures, central Cascadia subduction zone. In: Rogers, A.M., Walsh, T.J., Kockelman, W.J., Priest, G.R. (Eds.), Assessing earthquake hazards and reducing risk in the Pacific Northwest: U.S. Geological Survey Professional Paper 1560 vol. 1, pp. 91–114.
Nelson, A.R., Jennings, A.E., Kashima, K., 1996. An earthquake history derived from stratigraphic and microfossil evidence of relative sea-level change at Coos Bay, southern coastal Oregon. Geol. Soc. Am. Bull. 108, 141–154.
Nelson, A.R., Ota, Y., Umitsu, M., Kashima, K., Matsushima, Y., 1998. Seismic or hydrodynamic control of rapid late-Holocene sea-level rises in southern coastal Oregon, USA? The Holocene 8, 287–299.
Ouimet, W.B., Whipple, K.X., Granger, D.E., 2009. Beyond threshold hillslopes: Channel adjustment to base-level fall in tectonically active mountain ranges. Geology 37, 579–582.
Pavlis, T.L., Bruhn, R.L., 1983. Deep-seated flow as a mechanism for the uplift of broad forearc ridges and its role in the exposure of high P/T metamorphic terranes. Tectonics 2, 473–497.
Perron, J.T., Royden, L., 2013. An integral approach to bedrock river profile analysis. Earth Surf. Process. Landf. 38, 570–576.
Personius, S.F., 1995. Late Quaternary stream incision and uplift in the forearc of the Cascadia subduction zone, western Oregon. J. Geophys. Res. http://dx.doi.org/10.1029/95JB01684.
Peterson, C., Darienzo, M., 1989. Episodic, abrupt tectonic subsidence recorded in late Holocene deposits of the South Slough syncline: An on-land expression of shelf fold belt deformation from the southern Cascadia margin. Geological Society of America Abstracts with Programs, p. 129.
Porrit, R.W., Allen, R.M., Boyarko, D.C., Brudzinski, M.R., 2011. Investigation of Cascadia segmentation with ambient noise tomography. Earth Planet. Sci. Lett. 309. http://dx.doi.org/10.1016/j.epsl.2011.06.026.

Prancevic, J.P., Lamb, M.P., Fuller, B.M., 2014. Incipient sediment motion across the river to debris-flow transition. Geology 42 (3), 191–194.
Reneau, S.L., Dietrich, W.E., 1991. Erosion rates in the southern Oregon Coast Range: Evidence for an equilibrium between hillslope erosion and sediment yield. Earth Surf. Process. Landf. 16, 307–322.
Roering, J.J., 2008. How well can hillslope evolution models "explain" topography? Simulating soil transport and production with high-resolution topographic data. Geol. Soc. Am. Bull. 120, 1248–1262.
Roering, J.J., Kirchner, J.W., Dietrich, W.E., 2005. Characterizing structural and lithologic controls on deep-seated landsliding: Implications for topographic relief and landscape evolution in the Oregon Coast Range, USA. Geol. Soc. Am. Bull. 117, 654–668.
Roering, J.J., Marshall, J., Booth, A.M., Mort, M., Jin, Q., 2010. Evidence for biotic controls on topography and soil production. Earth Planet. Sci. Lett. 298, 183–190.
Satake, K., Shimazaki, K., Tsuji, Y., Ueda, K., 1996. Time and size of a giant earthquake in Cascadia inferred from Japanese tsunami records of January 1700. Nature 379, 246–249.
Schmidt, K.M., Roering, J.J., Stock, J.D., Dietrich, W.E., Montgomery, D.R., Schaub, T., 2001. The variability of root cohesion as an influence on shallow landslide susceptibility in the Oregon Coast Range. Can. Geotech. J. 38 (5), 995–1024.
Schwanghart, W., Scherler, D., 2013. Short Communication: TopoToolbox 2 – an efficient and user-friendly tool for Earth surface sciences. Earth Surf. Dyn. Discuss. 1, 261–275.
Shelef, E., Hilley, G., 2016. Unified framework for modeling landscape evolution by discrete flows. J. Geophys. Res. http://dx.doi.org/10.1002/2015JF003693.
Shobe, C.M., Tucker, G.E., Anderson, R.S., 2016. Hillslope-derived blocks retard river incision. Geophys. Res. Lett. http://dx.doi.org/10.1002/2016GL069262.
Sklar, L.S., Dietrich, W.E., 2001. Sediment and rock strength controls on river incision into bedrock. Geology 29 (12), 1087–1090.
Sklar, L.S., Dietrich, W.E., 2004. A mechanistic model for river incision into bedrock by saltating bed load. Water Resour. Res. http://dx.doi.org/10.1029/2003WR002496.
Snavely, P.D., Wagner, H.C., MacLeod, N.S., 1964. Rhythmic-bedded eugeosynclinal deposits of the Tyee formation, Oregon Coast Range. Kansas Geol. Survey Bull. 169, 461–480.
Snyder, N.P., Whipple, K.X., Tucker, G.E., Merritts, D.J., 2000. Landscape response to tectonic forcing: Digital elevation model analysis of stream profiles in the Mendocino triple junction region, northern California. Geol. Soc. Am. Bull. 112, 1250–1263.
Snyder, N.P., Whipple, K.X., Tucker, G.E., Merritts, D.J., 2003. Importance of a stochastic distribution of floods and erosion thresholds in the bedrock river incision problem. J. Geophys. Res. http://dx.doi.org/10.1029/2001JB001655.
Stock, J., Dietrich, W.E., 2003. Valley incision by debris flows: Evidence of a topographic signature. Water Resour. Res. http://dx.doi.org/10.1029/2001WR001057.
Stock, J.D., Dietrich, W.E., 2006. Erosion of steepland valleys by debris flows. Geol. Soc. Am. Bull. 118, 1125–1148.
Sweeney, K.E., Roering, J.J., 2016. Rapid fluvial incision of a late Holocene lava flow: Insights from LiDAR, alluvial stratigraphy, and numerical modeling. Geol. Soc. Am. Bull. http://dx.doi.org/10.1130/B31537.1.
Sweeney, K.E., Roering, J.J., Ellis, C., 2015. Experimental evidence for hillslope control of landscape scale. Science 349 (6243), 51–53.
Thatcher, W., 1984. The earthquake deformation cycle, recurrence, and the time-predictable model. J. Geophys. Res. http://dx.doi.org/10.1029/JB089iB07p05674.
Tucker, G.E., Bras, R.L., 1998. Hillslope processes, drainage density, and landscape morphology. Water Resour. Res. 34, 2751–2764.
vanLaningham, S., Meigs, A., Goldfinger, C., 2006. The effects of rock uplift and rock resistance on river morphology in a subduction zone forearc, Oregon, USA. Earth Surf. Process. Landf. 31 (10), 1257–1279.
Wang, K., Tréhu, A.M., 2016. Invited review paper: Some outstanding issues in the study of great megathrust earthquakes—The Cascadia example. J. Geodyn. 98, 1–18.
Wang, K., Hu, Y., He, J., 2012. Deformation cycles of subduction earthquakes in a viscoelastic Earth. Nature 484, 327–332.
Wang, P.L., Engelhart, S.E., Wang, K., Hawkes, A.D., Horton, B.P., Nelson, A.R., Witter, R.C., 2013. Heterogeneous rupture in the great Cascadia earthquake of 1700 inferred from coastal subsidence estimates. J. Geophys. Res. Solid Earth 118 (5), 2460–2473.
Wesson, R.L., Melnick, D., Cisternas, M., Moreno, M., Ely, L.L., 2015. Vertical deformation through a complete seismic cycle at Isla Santa Maria, Chile. Nat. Geosci. 8 (7), 547–551.
Whipple, K.X., 2004. Bedrock rivers and the geomorphology of active orogens. Annu. Rev. Earth Planet. Sci. 32, 151–185.
Whipple, K.X., Tucker, G.E., 1999. Dynamics of the stream-power river incision model: Implications for height limits of mountain ranges, landscape response timescales, and research needs. J. Geophys. Res. Solid Earth 104, 17661–17674 (1978–2012).
Whittaker, A.C., Cowie, P.A., Attal, M., Tucker, G.E., Roberts, G.P., 2007. Contrasting transient and steady-state rivers crossing active normal faults: New field observations from the Central Apennines, Italy. Basin Res. 19, 529–556.
Willett, S.D., McCoy, S.W., Perron, J.T., Goren, L., Chen, C.Y., 2014. Dynamic reorganization of river basins. Science http://dx.doi.org/10.1126/science.1248765.
Witter, R.C., Kelsey, H.M., Hemphill-Haley, E., 2003. Great Cascadia earthquakes and tsunamis of the past 6700 years, Coquille River estuary, southern coastal Oregon. Geol. Soc. Am. Bull. 115, 1289–1306.
Wobus, C., Whipple, K.X., Kirby, E., Snyder, N., Johnson, J., Spyropolou, K., Crosby, B., Sheehan, D., 2006. Tectonics from topography: Procedures, promise, and pitfalls. Geol. Soc. Am. Spec. Pap. 398, 55–74.